


Laser Synthetic Aperture Coherent Imaging for Micro-Rotating Objects Based on Array Detectors

Anjing Cui, Daojing Li , Jiang Wu, Jinghan Gao, Kai Zhou, and Bo Liu

Abstract—Through the relative motion of ladar and object, inverse synthetic aperture ladar can form the virtual synthetic aperture and improve the imaging resolution. On the basis of coherent array detectors with the laser local oscillator, the problem of laser synthetic aperture coherent imaging for micro-rotating objects is studied. Firstly, structure and parameters of the telescope system based on the diffractive optical system are introduced. Then, the signal model of the imaging method is built, the imaging method is proposed, and influence of noise is analyzed. Afterwards, the signal model of the vibrating object is established and the vibration phase compensation method is proposed. The imaging method proposed forms a virtual aperture through micro-rotation of the object, and realizes high-resolution imaging in the pitch direction and azimuth direction. Without transmitting or processing broadband signals, the imaging system is easy to realize in engineering, and simulation results verify the effectiveness of the imaging method. Meanwhile, Fourier ptychography in the far-field condition is analyzed, and characteristics of the two methods are compared. It is concluded that the imaging method proposed belongs to the concept of traditional matched filter coherent imaging while far-field Fourier ptychography is classified into the category of super-resolution imaging.

Index Terms—Laser synthetic aperture coherent imaging, coherent array detectors, laser local oscillator, inverse synthetic aperture ladar, diffractive optical system, fourier ptychography.

I. INTRODUCTION

IN MICROWAVE imaging, radar with a large aperture can improve the resolution of images. Through the relative motion of ladar and object, inverse synthetic aperture radar (ISAR) receives the echo signal by small aperture, and high-resolution imaging of large aperture radar is realized with the echo signal processed [1].

Manuscript received 10 September 2022; revised 16 November 2022; accepted 25 November 2022. Date of publication 29 November 2022; date of current version 7 December 2022. This work was supported by the Key Deploy Projects of Chinese Academy of Sciences under Grant E03701010F. (*Corresponding author: Daojing Li.*)

Anjing Cui, Jiang Wu, Jinghan Gao, and Kai Zhou are with the National Key Lab of Microwave Imaging Technology, Aerospace Information Research Institute, Chinese Academy of Sciences, Beijing 100190, China, and also with the School of Electronic, Electrical and Communication Engineering, University of Chinese Academy of Sciences, Beijing 100049, China (e-mail: cuianjing20@mails.ucas.ac.cn; 15074736402@163.com; gaojinghan20@mails.ucas.ac.cn; zk_6810@163.com).

Daojing Li is with the National Key Lab of Microwave Imaging Technology, Aerospace Information Research Institute, Chinese Academy of Sciences, Beijing 100190, China (e-mail: lidj@mail.ie.ac.cn).

Bo Liu is with the China Academy of Aerospace Science and Innovation, Beijing 100176, China (e-mail: lynnandsky@163.com).

Digital Object Identifier 10.1109/JPHOT.2022.3225468

With characteristics of the laser band similar to that of the microwave band, a large-aperture telescope enables high-resolution imaging, and the angular resolution of the telescope is limited by the aperture. Because of difficulties in manufacture, platform, and so on, Synthetic Aperture Ladar (SAL) and Inverse Synthetic Aperture Ladar (ISAL) are often applied to improve imaging resolution. With the object (high-reflectivity Lockheed Martin star logo) 1.6 km away, Lockheed Martin Coherent Technologies completed the demonstration of SAL imaging from an airborne platform in 2011, and the cross-range resolution reached 2.5 cm [2]. In 2017, ISAL imaging for the 1 km-away airplane model was completed by Institute of Electronics, Chinese Academy of Science (IECAS) [3]. In 2018, Shanghai Aerospace Electronics Technology Institute and Shanghai Jiao Tong University carried out the ISAL outdoor experiment, which used phase-coded continuous wave signal and realized 3 cm-resolution imaging for the 200 m-away object [4]. In 2019, an autofocus algorithm was proposed to compensate for the phase error introduced by translational and rotational micro-vibrations of objects, and the 80 m-away satellite model was imaged, whose angular rate was 17.5 mrad/s [5]. With a 2 km-away satellite model being the object and a viewing angle change of less than 180°, a 3-D ISAL imaging experiment was carried out by IECAS in 2020 [6]. Based on narrow-pulse laser signal, Aerospace Information Research Institute, Chinese Academy of Sciences completed ISAL imaging of the 83 m-away cooperative object and the 165 m-away non-cooperative object in 2021, and the resolution of the imaging results was better than that of the real aperture corresponding to the beamwidth [7]. In the case of a large squint angle, the institute realized ISAL imaging of the cooperative object by binary phase shift keying (BPSK) signal and compensated for the motion phase error in 2022 [8].

Based on the concept of traditional ISAL, which images in range direction and azimuth direction, the feasibility of the scheme that ISAL with Coherent Array Detectors (CAD) images in the pitch direction and azimuth direction is analyzed, and the Laser Synthetic Aperture Coherent (LSAC) imaging method based on the array detectors is introduced. The method forms the virtual synthetic aperture through the micro-rotation of the object and improves the resolution of imaging results. Without transmitting or processing wideband signals, the method has the characteristics of a simple system and a close combination of existing optical systems. At the same time, the method proposed and Fourier Ptychographic (FP) imaging are compared from the perspective of imaging resolution.

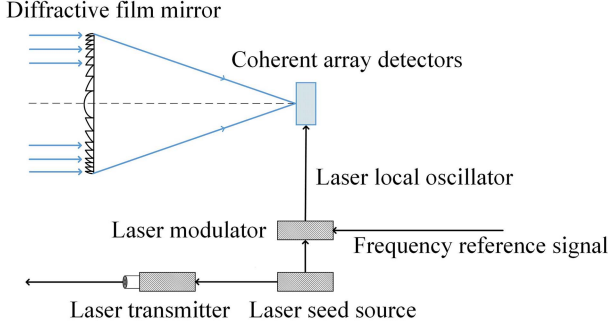


Fig. 1. Structure of the LSAC system.

II. LASER SYNTHETIC APERTURE COHERENT IMAGING

A. Coherent Array Detectors and System Structure

CADs with a Laser Local Oscillator (LLO) are applied in LSAC. Taking the CADs released by Pointcloud Incorporated in 2020 via silicon photonic elements and a network of silicon waveguides [9] as an example, the laser center wavelength is $1.55 \mu\text{m}$, the detector scale is 32×16 , the size of the detector is $8 \mu\text{m} \times 5 \mu\text{m}$, and CADs obtain complex images with phase information through heterodyne detection. Another method to realize coherent detection is optical path mixing in space between the LLO and the echo signal, which can also be used in holographic imaging [10], [11] and laser complex imaging processing [12]. The current research basis of LLO and CADs makes LSAC possible.

The LSAC system structure with diffractive film mirror [13], [14] is shown in Fig. 1. The CADs are set at the focal plane of the telescope. The narrow-band laser signal of the laser seed source is amplified to form the laser transmitting signal, and the signal is modulated by the electronic frequency reference signal (such as 10 MHz) to form the LLO. The echo signal and LLO are received by the detectors and converted into the digital signal by an Analog-Digital Converter (ADC), which prepares it for coherent imaging processing. The result of LSAC is in the pitch direction and azimuth direction. With range resolution uninvolved, the structure and imaging effect of the system are similar to those of traditional optical imaging systems. Without broadband transmitting signals, the CADs with LLO reduce the amount of equipment, simplify the system, and lay a foundation for 2-D synthetic aperture imaging.

In this paper, the laser wavelength is set as $1.55 \mu\text{m}$, the detector scale is 64×64 , and the detector size is $8 \mu\text{m} \times 8 \mu\text{m}$.

B. Model of Laser Echo Signal

A schematic diagram of LSAC for the micro-rotating object is shown in Fig. 2. Assume that the 3-D satellite and the point array rotate around X' axis and Y' axis at the same time, which are parallel axis and Y axis. The center of the telescope coincides with the origin of the coordinate axis, and the distance between the center of the object and the telescope is R_0 .

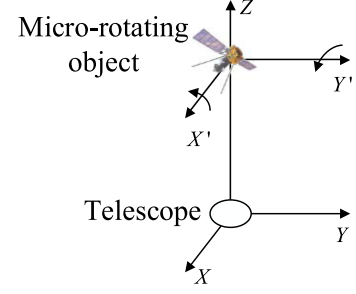


Fig. 2. Schematic diagram of LSAC for micro-rotating object.

As illustrated in [15], [16], [17], when the frequency of CADs collecting complex images is high enough, the changes of the rotating axis vector and rotating angular velocity of the object can be ignored within the time interval, and the coordinate change of the i -th point of the object is

$$\begin{bmatrix} x_i(t) \\ y_i(t) \\ z_i(t) \end{bmatrix} \approx W \left(\vec{\Omega}_x, \omega_x(t - 1/f_s) \right) \cdot W \left(\vec{\Omega}_y, \omega_y(t - 1/f_s) \right) \cdot \begin{bmatrix} x_i(t - 1/f_s) \\ y_i(t - 1/f_s) \\ z_i(t - 1/f_s) \end{bmatrix} \quad (1)$$

where $\omega_x(t)$ and $\omega_y(t)$ are the angular velocities of the object rotation about the x and y axes, f_s is the slow-time sampling frequency of CADs, $\vec{\Omega}_x$ and $\vec{\Omega}_y$ are rotation axis vectors, and W is the transformation matrix of the coordinate.

With the bistatic imaging system, the laser is transmitted with a wide beam, and CADs receive the echo signal of the large field of view. When the array detectors collect low-resolution images, set the echo signal of the rotating object to be

$$s(x, y, t) = \sum_i^{N_t} \text{rect} \left[\frac{t - R_i(x, y, t)/c}{\tau} \right] \exp \left\{ -j \frac{2\pi}{\lambda} R_i(x, y, t) \right\} \quad (2)$$

$$R_i(x, y, t) = R_t(t) + R_r(x, y, t) \quad (3)$$

$$R_t(t) = \sqrt{[x_i(t) - x_t]^2 + [y_i(t) - y_t]^2 + [z_i(t) - z_t]^2} \quad (4)$$

$$R_r(x, y, t) = \sqrt{[x_i(t) - x]^2 + [y_i(t) - y]^2 + z_i^2(t)} \quad (5)$$

where N_t is the number of point objects, $(x_i(t), y_i(t), z_i(t))$ is the coordinate of the i -th point object, (x_t, y_t, z_t) is the coordinate of the laser transmitter, (x, y) the coordinate on the telescope plane, $R_t(t)$ is the distance between the laser transmitter and the i -th point object, $R_r(x, y, t)$ is the distance between the i -th point object and the telescope plane, $R_i(x, y, t)$ is the propagation distance of i -th point object's signal, τ is the fast-time pulse width of the laser transmitted, and λ is the center wavelength of the laser.

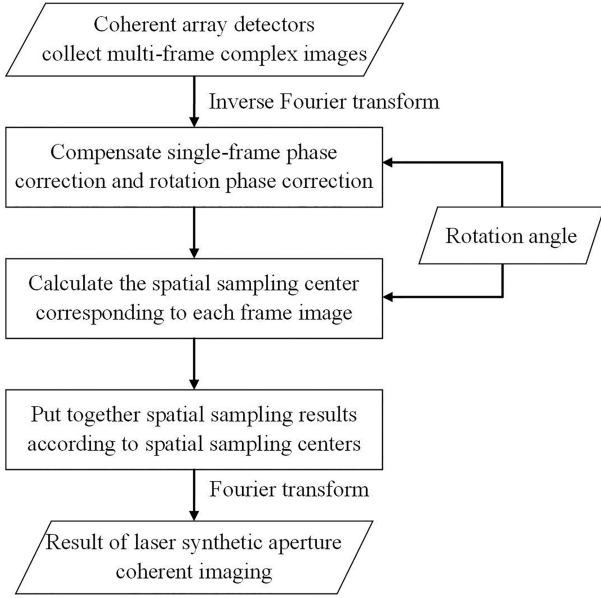


Fig. 3. The processing flow of LSAC for micro-rotating object.

Obviously, (2) describes the complex echo signal, which has a clear physical meaning. The echo signal is focused by the telescope and received by the CADs. Because of the limited bandwidth of the CADs, the output signal is equivalently low-pass filtered in the frequency domain.

C. Laser Synthetic Aperture Coherent Imaging for Micro-Rotating Object

1) *Imaging Process*: Generally, the attitude control accuracy of the low-orbit satellite is at the level of an arcsecond, and the attitude stability can reach $1.7 \mu\text{rad/s}$. Thus, the objectively existent 2-D micro-rotation of the object makes it feasible to realize high-resolution LSAC.

The process of LSAC for micro-rotating objects is shown in Fig. 3. CADs collect multi-frame images of the micro-rotating object. According to the rotation angle, compensate the single-frame phase and the rotation phase of the spatial sampling result (SSR) corresponding to each frame of complex image, and calculate the spatial sampling center. Then, put together SSRs of multi-frame complex images based on their spatial sampling centers, which enlarges the spatial sampling range equivalently, and the imaging resolution can be improved.

2) *Single-Frame Phase Correction and Rotation Phase Correction*: The SSR of the single-frame complex image collected by the CADs is on the telescope plane ($x-y$ plane). The distances between the object and different positions on the telescope plane vary, and the second-order phase of the SSR corresponding to each frame of complex image is caused. Single-frame phase correction is used to compensate for the following second-order phase in each SSR

$$\varphi_0(x, y) = \frac{2\pi}{\lambda} \left(\sqrt{x^2 + y^2 + R_0^2} - R_0 \right) \quad (6)$$

During the rotation of the object around X' axis and Y' axis, the change of distances between point objects and the center of the telescope varies. When the point object is located at the intersection of the two rotation axes (coordinate axis origin Fig. 2), the distance between the object and the center of the telescope remains unchanged. When the point object deviates from the intersection, the distance change is related to the distances between the object and the two rotation axes.

When the object rotates, to compensate for the phase caused by the distance change, the rotation phase correction is carried out for the corresponding SSR of each complex image. For the 3-D object, which consists of point objects, the distances between point objects and the intersection of the rotation axis are calculated, and the point object located at the mean of the distance is set to be the reference. During the rotation, the varying distance between the reference point object and the center of the telescope is calculated, the rotation phase generated by the varying distance is applied to the rotation phase correction, and the rotation phase is as follows

$$\varphi_r(t) = \frac{2\pi}{\lambda} \left\{ \sqrt{x_{mid}^2(t) + y_{mid}^2(t) + z_{mid}^2(t)} - \sqrt{x_{mid}^2\left(\frac{T}{2}\right) + y_{mid}^2\left(\frac{T}{2}\right) + z_{mid}^2\left(\frac{T}{2}\right)} \right\} \quad (7)$$

When the 3-D object rotates, $(x_{mid}(t), y_{mid}(t), z_{mid}(t))$ is the coordinate of the reference point object, and T is the slow-time duration of the CADs collecting complex images.

3) *Resolution of the Single-Frame Complex Image*: Assume that size of the detector is a , the focal length and aperture of the telescope are f and D . The far-field condition requires that the object distance R_0 satisfy

$$R_0 \geq 2D^2/\lambda \quad (8)$$

In the far field condition, the resolutions corresponding to the detector size of the system and the diffraction limit of the telescope are $\rho_a = aR_0/f$ and $\rho_e = 1.22\lambda R_0/D$ respectively. It is usually that $\rho_a > \rho_e$.

According to the resolution formula that

$$\rho = \frac{\lambda}{\theta} \quad (9)$$

$$\theta = \arctan\left(\frac{|d|}{R_0}\right) \approx \frac{|d|}{R_0} \quad (10)$$

where $|d|$ represents the corresponding spatial sampling range of the image. $|d_a| = \lambda f/a$ and $|d_e| = D/1.22$ are spatial sampling ranges corresponding to images with resolutions of ρ_a and ρ_e .

When the imaging resolution reaches ρ_e , the spatial sampling range satisfies that

$$x^2 + y^2 \leq \left(\frac{d_e}{2}\right)^2 \quad (11)$$

In this case, the size of the detector is required to meet

$$a \leq f \frac{\lambda}{D} = \lambda F\# \quad (12)$$

where $F_{\#}$ represents the f-number of the optical system. The condition above can be reached when the long-focal length system is adopted, otherwise, it is equivalent to reducing the range of the corresponding spatial to

$$x^2 + y^2 \leq \left(\frac{d_a}{2}\right)^2 \quad (13)$$

When the imaging resolution is limited by the size of the detector, increasing the aperture of the telescope can improve the Signal to Noise Ratio (SNR) of the imaging results.

4) *Resolution Analysis of Laser Synthetic Aperture Coherent Imaging*: It is assumed that the object rotates around the X' axis and the Y' axis. Since the object rotation is equivalent to the synchronous rotation of the laser transmitter and the telescope, the spatial sampling center of the complex image collected by the CADs is determined by twice the rotation angle of the object.

When the object rotates around the X' axis and the Y' axis at angles $\Delta\theta_x$ and $\Delta\theta_y$, the CADs collect the complex image, and the corresponding spatial sampling center is $(2\Delta\theta_y R_0, 2\Delta\theta_x R_0)$. If the CADs collect multi-frame images in the process of object rotation, the spatial sampling range of LSAC in the X direction and the Y direction can be increased as

$$|d_u| = |d_0| + 2\Delta\theta_u R_0 \quad (14)$$

the resolution of LSAC reaches

$$\rho_u = \frac{\lambda R_0}{|d_u|} \quad (15)$$

where u represents X or Y , and $|d_0|$ is the spatial sampling range of the single-frame complex image. With $|d_u| \geq |d_0|$, it is obvious that LSAC can improve imaging resolution through object micro-rotation.

D. Simulation of Laser Synthetic Aperture Coherent Imaging

When the slow-time sampling rate of the CADs is low, corresponding SSRs of complex images collected are nonoverlapping. The simulation parameters of LSAC for micro-rotating objects are listed in Table I, the resolution of the single-frame complex image collected by CADs is about 4 times lower than that corresponding to the diffraction limit of the telescope, and the system meets the far-field condition. During collecting a single-frame complex image, the fast-time receiving duration of each coherent detector in the array is $1.5 \mu\text{s}$, and each pixel of the image is the mean of the fast-time laser echo signal, which is equivalent to processing the fast-time signal with a low-pass filter with 1 MHz bandwidth.

As shown in Fig. 4, the $50 \text{ m} \times 50 \text{ m} \times 50 \text{ m}$ 3-D satellite and 3×3 point array are set to be the observation objects of LSAC. When the spacing of the point array is 0.3 m, the single-frame complex image and the corresponding SSR collected by CADs at the initial time are shown in Fig. 5. Due to the focal length of the telescope and the size of the detector, the effective aperture (30 mm) is only one-quarter of telescope aperture. At this time, point objects with 0.3 m spacing cannot be distinguished in the single-frame image.

TABLE I
SIMULATION PARAMETERS OF LSAC FOR MICRO-ROTATING OBJECT

Parameters	Values
center wavelength of the laser	1.55 μm
detection distance	20 km
aperture of telescope	120 mm
focal length of telescope	150 mm
size of detector	8 $\mu\text{m} \times 8 \mu\text{m}$
detector scale	64 \times 64
field of view	68.3 m \times 68.3 m
effective aperture of telescope	30 mm
corresponding angle of telescope effective aperture	1.5 μrad
fast-time sampling frequency of detector	20 MHz
pulse width of laser transmitted	1 μs
fast-time receiving duration of detector	1.5 μs
diffraction limit of telescope	15.76 μrad
resolution corresponding to the diffraction limit	0.32 m
angular resolution corresponding to detector size	53.33 μrad
resolution corresponding to detector size	1.07 m
ratio of resolution corresponding to detector size and diffraction limit	3.38
number of complex images	13
angle of the object rotating around x'/y' axis during collecting 2 complex images	0.53 μrad
total angle of the object rotating around x'/y' axis	6.36 μrad
spatial sampling range of LSAC in x/y direction	0.28 m
resolution of LSAC in x/y direction	0.11 m

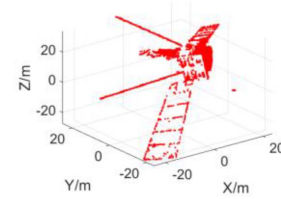


Fig. 4. 3-D satellite and 3×3 point array.

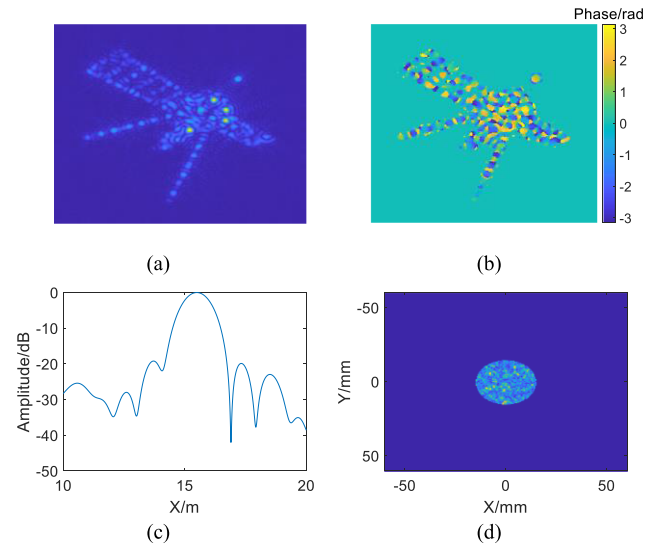


Fig. 5. The single-frame complex image and the corresponding SSR. (a) Magnitude of the complex image; (b) Phase of the complex image; (c) Slice of the point array imaging; (d) Corresponding SSR.

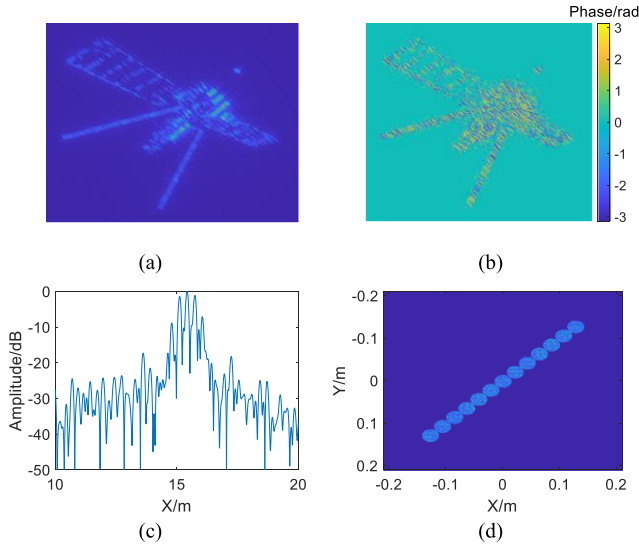


Fig. 6. The LSAC result and the nonoverlapping SSR. (a) Magnitude of the LSAC result; (b) Phase of the LSAC result; (c) Point array imaging slice of the LSAC result; (d) Corresponding SSR of the LSAC result.

Based on 13 frames of complex images, the LSAC result and the corresponding SSR are shown in Fig. 6, and the corresponding SSR of each frame of complex images does not overlap. Compared with the single-frame complex image, the resolution of the LSAC result in the X direction and the Y direction increase by 9 times in theory, and point objects with 0.3 m spacing can be distinguished.

When the slow-time sampling rate of the CADs is increased, which makes the corresponding SSRs of 2 complex images overlap by 75%, 49 frames of complex images are needed to improve the resolution of the LSAC result by 9 times. During the CADs collecting 2 complex images, the angle of the object rotating around the X' axis and the Y' axis is $0.13 \mu\text{rad}$, and the total angle of the object rotating around the X' axis and the Y' axis is $6.36 \mu\text{rad}$. The spatial sampling range and resolutions of LSAC in the X direction and Y direction are 0.28 m and 0.11 m, respectively. With a 75% overlapping ratio of the SSRs corresponding to multi-frame complex images, the LSAC result and the spatial sample result are shown in Fig. 7, and the point objects with 0.3 m spacing can be distinguished. Comparing Figs. 6(d) and 7(d), it can be found that the increase of the overlapping ratio requires more images to be used in LSAC with the resolution of the imaging results maintained, which is conducive to the sidelobe suppression of imaging results.

E. Influence Analysis of Noise and Object Vibration

Noise of laser echo signal, object vibration and other factors lead to defocus of imaging results in ISAL, and LSAC also faces these problems. The influence of noise on imaging and the compensation method of vibration phase are analyzed below.

1) *Analysis of Noise Influence:* When the SNR of multi-frame complex images collected by CADs is 5 dB, LSAC results with 0 and 75% overlapping rates of SSRs are shown in Fig. 8(a)–(c) and (d)–(f). The simulation results indicate

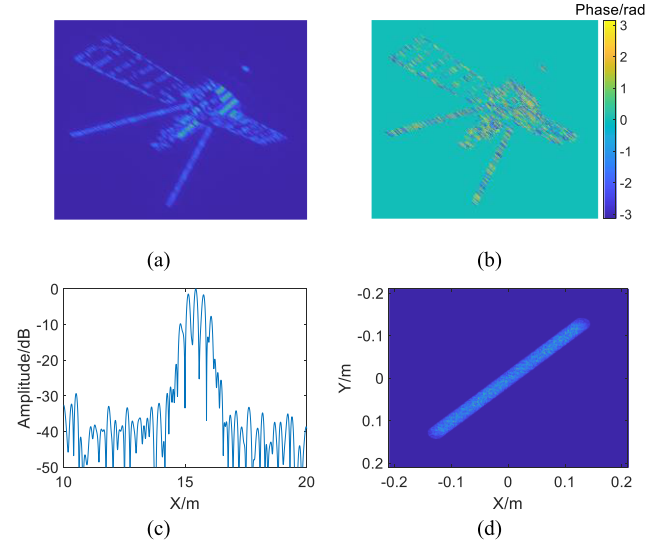


Fig. 7. The LSAC result and the SSR with a 75% overlapping ratio. (a) Magnitude of the LSAC result; (b) Phase of the LSAC result; (c) Point array imaging slice of the LSAC result; (d) Corresponding SSR of the LSAC result.

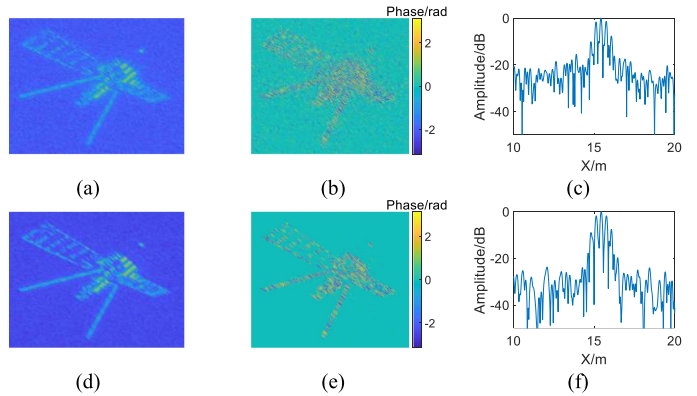


Fig. 8. LSAC results when the SNR of single-frame complex images is 5 dB. (a)–(c) are the LSAC results when 13 frames of complex images with nonoverlapping SSRs are applied, (d)–(f) are the LSAC results when 49 frames of complex images with 75% SSR overlapping rate are applied. (a) and (d) are magnitude of LSAC results, (b) and (e) are phase of LSAC results, (c) and (f) are point array imaging slice of LSAC results.

that when 13 frames of complex images with nonoverlapping SSRs are applied, SNR of the LSAC result is about 20 dB, and the SNR of the imaging result with the same resolution is improved to around 30 dB if 49 frames of complex images with 75% SSR overlapping rate are applied. Thus the increase of the overlapping rate and the number of complex images can reduce the influence of noise and improve the SNR of LSAC results.

2) *Vibration Phase Compensation:* In practical applications, vibration of the object may lead LSAC results defocusing. A simplified model of the vibrating object is constructed and the vibration phase compensation method from the perspective of SSRs are analyzed below.

Parameters of LSAC are listed in Table I, the number of complex images and the overlapping rate of corresponding SSRs

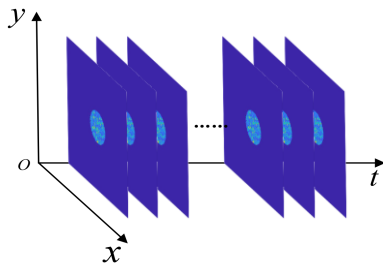


Fig. 9. Schematic diagram of the 3-D matrix constructed by SSRs corresponding to multi-frame images.

are 49 and 75% respectively, the sampling duration of CADs is set at 2 s with 24 Hz slow-time sampling frequency. The ideal LSAC results are shown in Fig. 7. As presented in Fig. 9, SSRs of multi-frame complex images can construct a 3-D matrix in pitch (x)-azimuth (y)-time (t) direction, which makes it possible to estimate the vibration phase.

Based on the schematic diagram of LSAC shown in Fig. 2, it is assumed that the object is rigid and vibrates sinusoidally in z direction, with $0.3 \mu\text{m}$ amplitude and 5 Hz frequency, and the vibration phase can be compensated through processing the 3-D matrix in time direction shown in Fig. 9. The processing flow of vibration phase compensation is as follows.

- With vibration phase in pitch-azimuth direction similar, the mean values of the 3-D matrix can be taken in pitch-azimuth direction and a 1-D echo signal is formed.
- Under the condition that parameters of the micro-rotating object have been estimated, calculate the vibration phase of the 1-D echo signal through Space Correlation Algorithm (SCA) [18], and compensate phase of the 3-D matrix in time direction.

The spectrum comparison of the micro-rotation phase, the vibration phase and the echo signal phase is shown in Fig. 10(a), and it can be found that the frequency of the micro-rotation phase is lower than that of the vibration phase. The estimated vibration phase curve and LSAC results before/after phase compensation are presented in Fig. 10(b)–(d), and the vibration phase compensation makes entropy of the LSAC result drops from 11.3286 to 10.3554.

III. FOURIER PTYCHOGRAPHY AND IMAGING METHOD COMPARISON

A. Fourier Ptychography

Zheng et al. [19], [20] proposed Fourier Ptychography Microscopy (FPM) in 2013. Through illuminating the object from different angles with a simple Light-Emitting Diode (LED) matrix and receiving images with microscopy, the method enlarges the Numerical Aperture (NA) and the spatial sampling range equivalently, so as to improve the imaging resolution.

The spatial sampling center of the images collected can be changed by irradiating the object from different angles or receiving setting the microscopy in various locations. Dong et al. [21] proposed aperture-scanning Fourier ptychography in 2014. The application range of Fourier ptychography (FP) is extended from

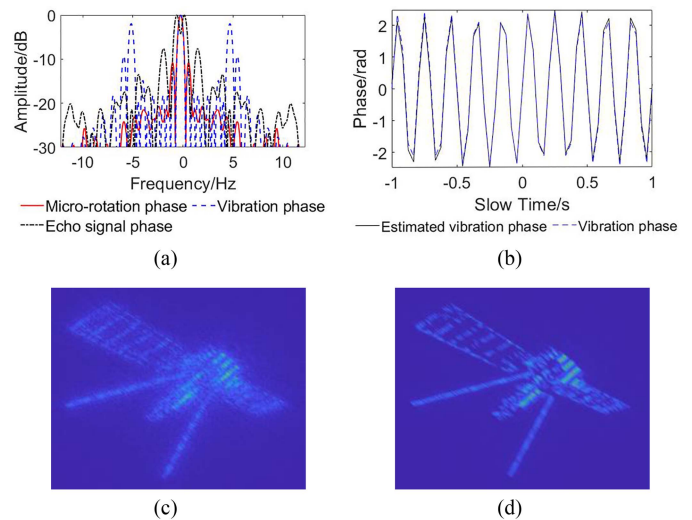


Fig. 10. Phase spectrum comparison, vibration phase estimation and LSAC results before/after vibration phase compensation. (a) Spectrum comparison of the micro-rotation phase, the vibration phase and the echo signal phase; (b) Comparison of the estimated vibration phase and the actual vibration phase; (c) the LSAC result before vibration phase compensation; (d) the LSAC result after vibration phase compensation.

microscopy to telescope, and the detection distance is increased to 0.7 m. Pacheco et al. [22] studied the Fourier ptychography technique aimed at the reflective system. On the basis of the movement of a large f -number lens, [23] solved the problem of FP with a low overlapping ratio. Xiang et al. [24] completed the reflective FP experiment base on the LED matrix and intended to apply FP to remote sensing in space. In the application scheme, a virtual aperture is formed by moving the laser transmitter, so as to increase the NA, and improve the imaging resolution.

1) *Fourier Ptychography Based on Multi-Frame Low-Resolution Images*: FP has been widely applied in high-resolution near-field microscopic imaging, and the method collects the light intensity of the images by Charge-Coupled Devices (CCD). Parameters of the system are listed in Table I, and the overlapping ratio of the corresponding SSRs of complex images is set to be 75% in the far-field condition. In order to enlarge the spatial sampling range and increase the imaging resolution by 9 times, 49 frames of images without phase information are collected by CCDs.

Based on multi-frame images, the FP results and the corresponding SSRs of the object consisting of a 3-D satellite and the 3×3 point array with $0.3/1.8$ m spacing are shown in Figs. 11 and 12. It is obvious that neither of the single-frame image nor the FP result can distinguish the point objects with 0.3 m spacing. However, when the spacing is increased to 1.8 m, the point objects can be distinguished in both the single-frame image and the FP result.

2) *Fourier Ptychography Based on a Single-Frame Low-Resolution Image*: In the object rotating process above, multi-frame images are collected by CCDs to be applied in FP, and the corresponding spatial sampling centers are determined by the rotating angle of the object. Since CCDs cannot collect the phase of images, and magnitude images are similar during the

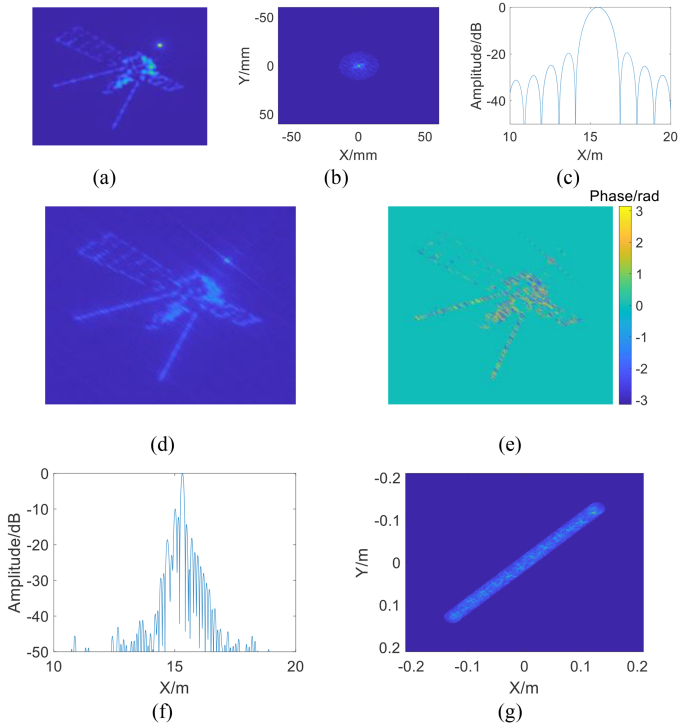


Fig. 11. The FP result based on multi-frame images and the corresponding SSR of the object consisting of a 3-D satellite and the 3×3 point array with 0.3 m spacing. (a) Magnitude of a single-frame image; (b) Spatial sampling of a single-frame image; (c) Point array imaging slice of a single-frame image; (d) Magnitude of the FP result; (e) Phase of the FP result; (f) Point array imaging slice of the FP result; (g) Corresponding SSR of the FP result.

micro-rotating process of the object in the far-field condition, it is difficult for multi-frame images to reflect the rotating information. Based on the simulations in the previous section, without altering the corresponding spatial sampling centers, replace multi-frame images with a single-frame image in FP. The FP results and the corresponding SSRs are shown in Fig. 13, and single-frame images are shown in Figs. 11(a) and 12(a).

Comparing Figs. 11 to 13, the imaging results based on multi-frame and single-frame low-resolution images are similar, thus FP in the far-field condition belongs to the category of super-resolution imaging methods.

B. Comparison and Discussion of Imaging Methods

According to the parameters listed in Table I, if the focal length of the telescope is increased to 600 mm, the resolution of images collected by the CADs can reach that corresponding to the diffraction limit of the telescope. Without the influence of noise and setting the 3-D satellite and 3×3 point array with 0.8 m spacing to be the object, the high-resolution image (corresponding to 600 mm focal length), the low-resolution image (corresponding to 150 mm focal length), the LSAC result based on 5 frames of complex images with the SSR nonoverlapping, the LSAC result based on 15 frames of complex images with SSR 75% overlapping, and the FP results based on 15-frame/single-frame magnitude image with the SSRs 75%

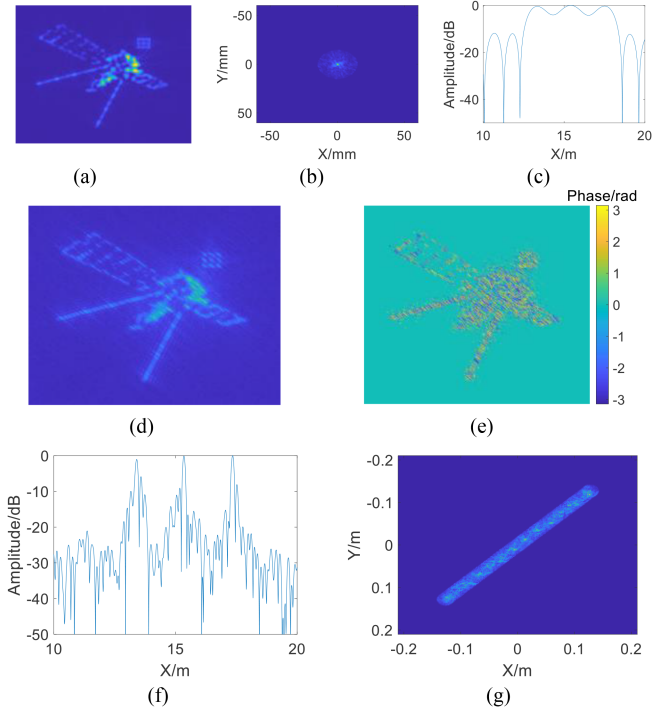


Fig. 12. The FP result based on multi-frame images and the corresponding SSR of the object consisting of a 3-D satellite and the 3×3 point array with 1.8 m spacing. (a) Magnitude of a single-frame image; (b) Spatial sampling of a single-frame image; (c) Point array imaging slice of a single-frame image; (d) Magnitude of the FP result; (e) Phase of the FP result; (f) Point array imaging slice of the FP result; (g) Corresponding SSR of the FP result.

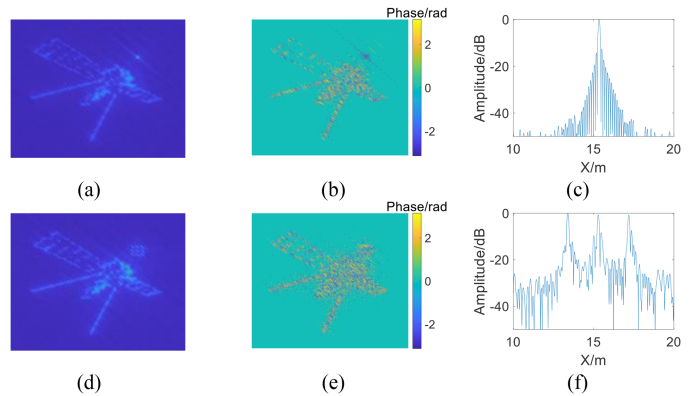


Fig. 13. The FP results based on a single-frame image. (a)–(c) are FP results of the object consisting of a 3-D satellite and the 3×3 point array with 0.3 m spacing. (d)–(f) are FP results of the object consisting of a 3-D satellite and the 3×3 point array with 1.8 m spacing. (a) and (d) are magnitude of FP results, (b) and (e) are phase of FP results, (c) and (f) are point array imaging slice of FP results.

overlapping are shown in Fig. 14. The low-resolution complex/magnitude images applied in LSAC/FP correspond to the telescope with 150 mm focal length. The spatial sampling range of the LSAC/FP result is 4 times larger than that of the low-resolution image. And the theoretical resolution of the LSAC results is close to that of the high-resolution image, which is 0.32 m.

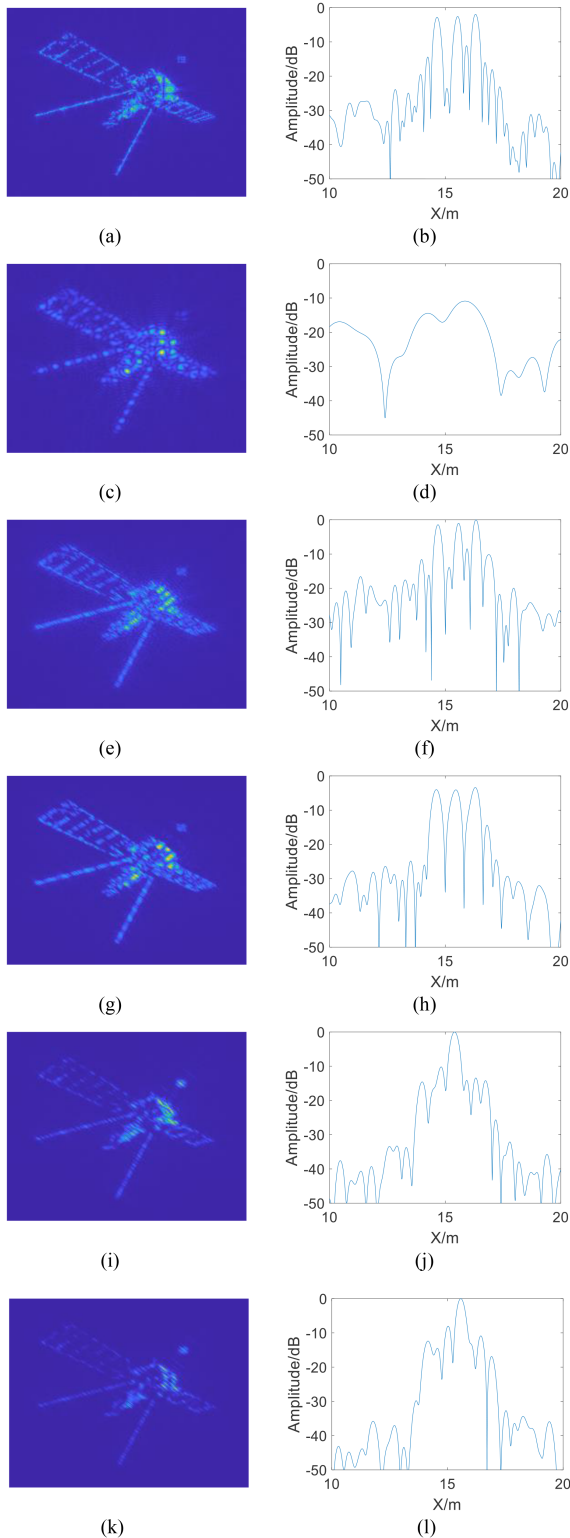


Fig. 14. Comparison of imaging methods. (a) and (b) are magnitude and point array imaging slice of high-resolution image; (c) and (d) are magnitude and point array imaging slice of low-resolution image; (e) and (f) are magnitude and point array imaging slice of the LSAC result with SSRs nonoverlapping; (g) and (h) are magnitude and point array imaging slice of the LSAC result with SSRs 75% overlapping; (i) and (j) are magnitude and point array imaging slice of the FP result based on multi-frame images; (k) and (l) are magnitude and point array imaging slice of the FP result based on single-frame image.

TABLE II
THE COMPARISON OF THE HIGH-RESOLUTION IMAGE, THE LOW-RESOLUTION IMAGE, THE LSAC RESULTS, AND THE FP RESULTS

image	distinguish the point array	correlation coefficient
the high-resolution image	yes	1
the low-resolution image	no	0.61
the LSAC result with SSRs nonoverlapping	yes	0.76
the LSAC result with SSRs 75% overlapping	yes	0.82
the FP result based on multi-frame images	no	0.66
the FP result based on a single-frame image	no	0.57

The comparison of the high-resolution image, the low-resolution image, the LSAC results, and the FP results are shown in Table II, where the correlation coefficients represent the similarity of the magnitude high-resolution image and other magnitude images.

According to Table II, LSAC can improve the image resolution effectively, and the imaging results' magnitudes are similar to that of the high-resolution images. When the overlapping ratio of the SSRs increases to 75%, which is realized by improving the slow-time sampling rate of the CADs, the number of complex images applied to LSAC enlarges, the sparsity of the SSRs decreases, and the correlation coefficients of the imaging results and the high-resolution image can be further improved.

Compared with the low-resolution image, the magnitudes of the FP result based on multi-frame images are more similar to that of the high-resolution image. In the far-field condition, although FP enlarges the spatial sampling range and reconstructs the phase of the imaging result, the phase may be different from that of the high-resolution complex image. Therefore, FP cannot improve imaging resolution effectively.

The complex images collected by the CADs have strict mathematical relation and definite physical meaning in the formation of laser synthetic aperture, which enables LSAC to reach high imaging resolution in principle and has important application value. In contrast, FP realizes 'phase reconstruction' and forms the complex image with overlapping SSRs of low-resolution magnitude images, and the system can be simplified through collecting magnitude images with CCDs. However, the high-resolution of the FP result is realized on the foundation that the multi-frame low-resolution images have a certain discrimination ability. With an uncertain reconstructed phase and unclear physical significance, the FP result is the numerical solution of the image in essence. FP does not belong to the traditional concept of coherent imaging based on matched filtering principle and should be classified into the category of super-resolution imaging.

IV. CONCLUSION

Based on the CADs with LLO, LSAC for the micro-rotating object is proposed in this paper, and the principle analysis and simulations of the imaging method are completed. Compared

with SAL/ISAL imaging, with the range resolution uninvolved, the result of LSAC is in pitch-azimuth direction and is similar to that of traditional optical imaging. Without applying broadband transmitting signal, LSAC has the characteristics of a simple system and less equipment.

When low-resolution images have a certain discrimination ability, FP can be one of the super-resolution imaging methods. While the essence of the FP result is the numerical solution, and the method differs from the traditional coherent imaging with matched filter. LSAC uses multi-frame complex images collected by the CADs, realizes high-resolution imaging in theory through forming large virtual synthetic aperture, which has strict mathematical relation and clear physical meaning. Compared with the telescope array, LSAC forms the virtual aperture by the micro-rotation of the object, which is a typical sparse model and leads to high sidelobe. The influence of the sidelobe on the imaging results can be suppressed by windowing.

The phase information of multi-frame complex images is the foundation of LSAC, and multiple factors will lead to the defocus of imaging results, such as vibration of the object, estimation error of object motion parameters and so on. In order to obtain accurate phase information, the vibration phase compensation method of the rigid object from the perspective of SSRs has been studied, and the vibration phase of the nonrigid object can be analyzed from the perspective of complex images. Since both LSAC and the vibration phase compensation in this paper are based on accurate estimation of object motion parameters, it is of great significance to carry out further research on object motion parameter estimation.

Disclosures: The authors declare no conflicts of interest.

Data available: Data underlying the results presented in this paper are not publicly available at this time but may be obtained from the authors upon reasonable request.

REFERENCES

- [1] M. Soumekh, "Cross-range imaging," in *Synthetic Aperture Radar Signal Processing With Matlab Algorithms*, 1st ed. Hoboken, NJ, USA: Wiley, 1999, pp. 73–95.
- [2] B. W. Krause et al., "Synthetic aperture lidar flight demonstration," in *Proc. CLEO: Laser Appl. to Photon. Appl.*, Optica Publishing Group, 2011, Paper PDPB7.
- [3] G. Li, N. Wang, D. Mo, R. Wang, Z. Zhang, and Y. Wu, "Inverse synthetic aperture lidar imaging with stepped-frequency continuous waveform," *Electron. Lett.*, vol. 53, no. 21, pp. 1424–1426, 2017.
- [4] X. Xu, S. Gao, and Z. Zhang, "Inverse synthetic aperture lidar demonstration and outdoor experiments," in *Proc. IEEE China Int. SAR Symp.*, 2018, pp. 1–4.
- [5] Z. Song, D. Mo, N. Wang, B. Li, Y. Shao, and R. Tan, "Inverse synthetic aperture lidar autofocus imaging algorithm for micro-vibrating satellites based on two prominent points," *Appl. Opt.*, vol. 58, no. 25, pp. 6775–6783, Sep. 2019.
- [6] D. Mo, Z. Song, B. Li, R. Wang, and Y. Wu, "Extended target three-dimensional reconstruction from inverse synthetic aperture lidar image sequence," *IEEE Geosci. Remote Sens. Lett.*, vol. 18, no. 3, pp. 548–552, Mar. 2021.
- [7] D. Li et al., "Multi-channel inverse synthetic aperture lidar imaging detection technology and experimental research," *Laser Optoelectron. Prog.*, vol. 58, no. 18, pp. 342–353, 2021.
- [8] A. Cui et al., "Moving target imaging of a dual-channel ISAL with binary phase shift keying signals and large squint angles," *Appl. Opt.*, vol. 61, no. 18, pp. 5466–5473, 2022.
- [9] C. Rogers et al., "A universal 3D imaging sensor on a silicon photonics platform," *Nature*, vol. 590, pp. 256–261, 2021.
- [10] U. Schnars and W. Jüptner, "Direct recording of holograms by a CCD target and numerical reconstruction," *Appl. Opt.*, vol. 33, no. 2, pp. 179–181, 1994.
- [11] A. Hussain, J. L. Martinez, and J. Campos, "Holographic superresolution using spatial light modulator," *J. Eur. Opt. Soc.: Rapid Pub.*, vol. 8, 2013.
- [12] A. Cui, D. Li, J. Wu, K. Zhou, and J. Gao, "Sparse sampling in frequency domain and laser imaging," *Acta Phys. Sinica*, vol. 71, no. 5, pp. 391–397, 2022.
- [13] D. Li, J. Gao, A. Cui, K. Zhou, and J. Wu, "Research on space-borne dual-wavelength land-sea Lidar system with 2 m diffractive aperture," *Chin. J. Lasers*, vol. 49, no. 3, pp. 123–134, 2022.
- [14] D. Li et al., "Laser application and sparse imaging analysis of diffractive optical system," *J. Radars*, vol. 9, no. 1, pp. 3974–3985, 2020.
- [15] X. Hu, D. Li, and J. Du, "Image processing for GEO object with 3D rotation based on ground-based InISAL with orthogonal baselines," *Appl. Opt.*, vol. 58, no. 15, pp. 3974–3985, May 2019.
- [16] G. Piovan and F. Bullo, "On coordinate-free rotation decomposition: Euler angles about arbitrary axes," *IEEE Trans. Robot.*, vol. 28, no. 3, pp. 728–733, Jun. 2012.
- [17] "Rotate a point about an arbitrary axis (3 dimensions)," 2002. [Online]. Available: <http://paulbourke.net/geometry/rotate/>
- [18] X. Hu, D. Li, J. Du, M. Ma, and J. Zhou, "Vibration estimation of synthetic aperture lidar based on division of inner view field by two detectors along track," in *Proc. IEEE Int. Geosci. Remote Sens. Symp.*, 2016, pp. 4561–4564.
- [19] G. Zheng, R. Horstmeyer, and C. Yang, "Wide-field, high-resolution Fourier ptychographic microscopy," *Nature Photon.*, vol. 7, no. 9, pp. 739–745, Sep. 2013.
- [20] G. Zheng, "Breakthroughs in photonics 2013: Fourier ptychographic imaging," *IEEE Photon. J.*, vol. 6, no. 2, Apr. 2014, Art. no. 0701207, doi: 10.1109/JPHOT.2014.2308632.
- [21] S. Dong et al., "Aperture-scanning Fourier ptychography for 3D refocusing and super-resolution macroscopic imaging," *Opt. Exp.*, vol. 22, no. 11, pp. 13586–13599, Jun. 2014.
- [22] S. Pacheco, G. Zheng, and R. Liang, "Reflective Fourier ptychography," *Proc. SPIE*, vol. 21, 2016, Art. no. 26010.
- [23] J. Wu, F. Yang, and L. Cao, "Resolution enhancement of long-range imaging with sparse apertures," *Opt. Lasers Eng.*, vol. 155, 2022, Art. no. 107068.
- [24] M. Xiang et al., "Coherent synthetic aperture imaging for visible remote sensing via reflective Fourier ptychography," *Opt. Lett.*, vol. 46, pp. 29–32, 2021.